

# Carrier dynamics in Landau-quantized graphene featuring strong Auger scattering

Martin Mittendorff<sup>1,2,\*†</sup>, Florian Wendler<sup>3</sup>, Ermin Malic<sup>3</sup>, Andreas Knorr<sup>3</sup>, Milan Orlita<sup>4,5</sup>, Marek Potemski<sup>4</sup>, Claire Berger<sup>6,7</sup>, Walter A. de Heer<sup>6,8</sup>, Harald Schneider<sup>1</sup>, Manfred Helm<sup>1,2</sup> and Stephan Winnerl<sup>1\*</sup>

**The energy spectrum of common two-dimensional electron gases consists of a harmonic (that is, equidistant) ladder of Landau levels, thus preventing the possibility of optically addressing individual transitions. In graphene, however, owing to its non-harmonic spectrum, individual levels can be addressed selectively. Here, we report a time-resolved experiment directly pumping discrete Landau levels in graphene. Energetically degenerate Landau-level transitions from  $n = -1$  to  $n = 0$  and from  $n = 0$  to  $n = 1$  are distinguished by applying circularly polarized THz light. An analysis based on a microscopic theory shows that the zeroth Landau level is actually depleted by strong Auger scattering, even though it is optically pumped at the same time. The surprisingly strong electron–electron interaction responsible for this effect is directly evidenced through a sign reversal of the pump–probe signal.**

Transport experiments on graphene in magnetic fields have revealed a number of fascinating phenomena, such as quantum ratchet effects<sup>1</sup>, the Hofstadter butterfly<sup>2–4</sup> and the fractional quantum Hall effect<sup>5,6</sup>. The anomalous quantum Hall effect, which is a consequence of a Landau level (LL) at zero energy in graphene (Fig. 1a), is considered a hallmark of the Dirac-fermion nature of charge carriers in graphene<sup>7,8</sup>. The non-equidistant LL structure has been observed in various continuous-wave (cw) magneto-spectroscopy experiments<sup>9–12</sup>, which provided evidence for the Dirac-cone band structure at various energies<sup>10,11</sup>. Furthermore, this technique allows one to determine the Fermi velocity<sup>9</sup> and to identify graphene of extremely high quality<sup>12</sup>. The observation of a giant Faraday rotation of light passing through graphene in magnetic fields as well as the demonstration of tunable THz detectors highlight the application potential of graphene in magneto-optic devices<sup>13,14</sup>. For more sophisticated applications such as light emitters, however, a detailed knowledge of the carrier dynamics is required.

Although the relaxation dynamics in graphene at zero magnetic field has been studied intensively<sup>15–20</sup> there is so far only one time-resolved spectroscopy study in the presence of a magnetic field<sup>21</sup>, in which a pump probe study was performed at high energies corresponding to the excitation of a quasi-continuum of LLs characterized by a LL separation smaller than the LL broadening. The observed increase in relaxation time at enhanced magnetic fields was attributed to a suppression of Auger processes<sup>21</sup>. The role of Auger scattering bridging the valence and conduction bands and changing the number of charge carriers has been controversially discussed for graphene in the absence of magnetic fields<sup>19,22,23</sup>. Charge carriers fulfil energy and momentum conservation for Auger processes only along a straight line on the Dirac cone. It has been argued that the contribution of processes restricted to lines in

$k$ -space vanishes in the two-dimensional phase space. However, full quantum-mechanical treatments of the ultrafast carrier dynamics indicate that Auger processes, that is, Auger recombination and impact ionization, are very efficient in graphene<sup>19,24–26</sup>. The possibility of generating multiple electron–hole pairs due to impact ionization dominating over Auger recombination is at present a fascinating research topic. Although evidence for carrier multiplication was found in a pump–probe experiment<sup>19</sup>, two time- and angle-resolved photoemission spectroscopy studies do not report this effect<sup>27,28</sup>. However, the applied high pump fluence in the range of  $1 \text{ mJ cm}^{-2}$  in refs 27,28 results in a regime where Auger recombination is predicted to be predominant, preventing carrier multiplication from occurring<sup>25,26</sup>. Owing to their specific energy structure, the energetically lowest LLs, which can be selectively excited in the experiment, open a unique route to investigate the importance of Auger scattering in graphene.

In this Article, we present a joint experimental and theoretical study investigating the carrier dynamics in Landau-quantized graphene by selectively pumping and probing transitions between low-energy LLs. Hence, for the first time, the discrete graphene LL system is investigated in a time-resolved study. We apply radiation with a photon energy of 75 meV (wavelength: 16.5  $\mu\text{m}$ ) and magnetic fields of up to 7 T to address the possible relaxation channels of excited electrons in the presence of a magnetic field. Thorough understanding of the dynamics in this unique discrete-level system is obtained by performing pump–probe experiments with circularly polarized radiation, which allows one to selectively address the degenerate  $\text{LL}_{-1} \rightarrow \text{LL}_0$  and  $\text{LL}_0 \rightarrow \text{LL}_1$  transitions (Fig. 1a). Our main observation is that for one of the four possible combinations of pumping and probing with left- and right-circularly polarized radiation, the differential transmission signal (DTS) shows the opposite sign with respect to the signal

<sup>1</sup>Helmholtz-Zentrum Dresden-Rossendorf, PO Box 510119, 01314 Dresden, Germany. <sup>2</sup>Technische Universität Dresden, 01062 Dresden, Germany.

<sup>3</sup>Technische Universität Berlin, Hardenbergstraße 36, 10623 Berlin, Germany. <sup>4</sup>Laboratoire National des Champs Magnétiques Intenses, CNRS-UJF-UPS-INSA, 38042 Grenoble, France. <sup>5</sup>Charles University Faculty of Mathematics and Physics, Ke Karlovu 5, 121 16 Praha, Czech Republic.

<sup>6</sup>Georgia Institute of Technology, Atlanta, Georgia 30332, USA. <sup>7</sup>CNRS — Institut Néel, 38042 Grenoble, France. <sup>8</sup>Department of Physics, King Abdulaziz University, Jeddah 22254, Saudi Arabia. <sup>†</sup>Present address: University of Maryland, College Park, Maryland 20742, USA. \*e-mail: mhm@umd.edu; s.winnerl@hzdr.de

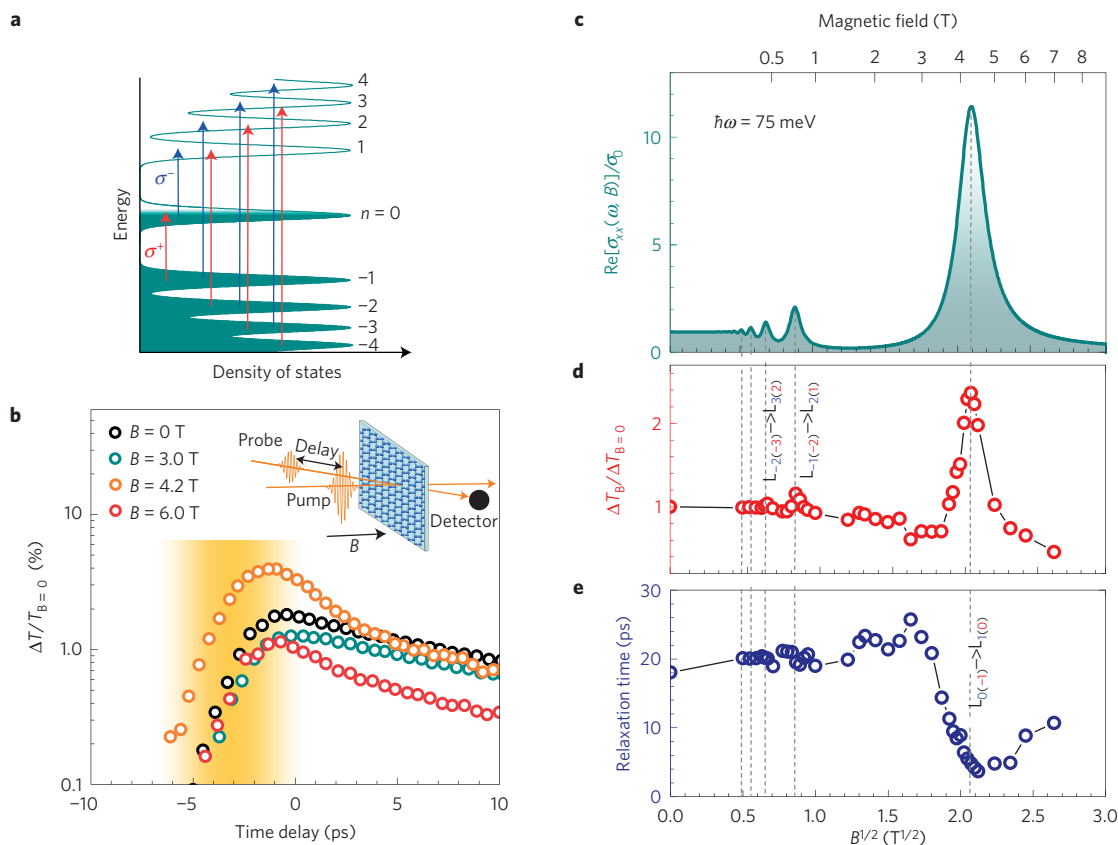


**Figure 1 | Pump-probe spectroscopy on graphene with linearly polarized radiation.** **a**, LL spectrum of graphene with allowed dipole transitions for  $\sigma^-$  and  $\sigma^+$ -radiation. **b**, Pump-probe signals for different magnetic fields. In the inset the pump-probe experiment involving linearly polarized beams is depicted. In this case, transitions allowed for  $\sigma^-$ -radiation as well as  $\sigma^+$ -radiation are excited and probed. **c**, Dynamic conductivity, which is proportional to the absorption, of one graphene layer. The calculation, as well as all experimental data in the other panels, corresponds to a photon energy of 75 meV. **d**,  $B$ -dependent pump-induced maximum transmission change normalized to the case at zero magnetic field. **e**, Initial decay time of the pump-probe signal for varied magnetic fields. For magnetic fields below 3 T this decay time corresponds to the slow component of the dynamics, whereas for higher fields it is dominated by the additional fast component. The dashed lines in **d** and **e** identify the corresponding LL transitions. Here the red (blue) subscripts denote transitions excited by  $\sigma^+$  ( $\sigma^-$ ) radiation, see also **a**.

expected from the usually applied single particle absorption bleaching scheme. This observation reveals a highly efficient elastic relaxation channel that we can unambiguously identify by performing microscopic time-resolved calculations of the carrier dynamics. The experiments and calculations show that Auger scattering is the predominant relaxation process giving rise to a redistribution of carriers in Landau-quantized graphene on a picosecond timescale. The fundamental insights obtained into the nature of carrier–carrier scattering in graphene in the presence of a magnetic field are relevant for novel applications, such as graphene-based Landau lasers.

The time-resolved experiments were performed on multilayer ( $\sim 40$  layers) epitaxial graphene (MEG) grown by thermal decomposition on the C-terminated face of SiC (ref. 29). The decoupled nature of the layers of the sample was evidenced by Raman spectroscopy<sup>30</sup> and cw magneto-spectroscopy<sup>9</sup>. The majority of graphene layers exhibit weak doping<sup>11,18</sup>, although layers close to the interface of SiC are strongly n-doped<sup>16,31,32</sup>. In our sample the majority of layers is n-type, with an electron concentration in the range of several  $10^{10} \text{ cm}^{-2}$  (see details of sample doping in Methods). The free-electron laser FELBE delivered radiation pulses with a duration of 2.7 ps (full-width at half-maximum, FWHM) and a photon energy of 75 meV. Various pump–probe experiments were performed, involving linear polarization as well as left- and right-circularly polarized radiation for pumping and probing. A simplified sketch of the experiment with linearly

polarized radiation is shown in the inset of Fig. 1b. Details on the experimental configuration can be found in the Methods. In all experiments, the sample temperature was kept at 10 K in a cryostat that allows the application of magnetic fields up to 7 T.

In the following, induced transmission transients (Fig. 1b) are analysed. The features of the induced transmission amplitudes (Fig. 1d) and the initial relaxation time (Fig. 1e) are identified by comparing their  $B$ -field dependence to the dynamic conductivity of a graphene layer (Fig. 1c). The dynamic conductivity, which is proportional to the absorption, is calculated using the Kubo formalism<sup>9</sup>, considering the dipole radiation selection rule  $|\Delta n| = 1$ . A width of 7 meV is chosen in accord with cw magneto-spectroscopy data<sup>11</sup>. The calculation allows us to attribute peaks in the induced transmission to the interband transitions  $LL_{-1(0)} \rightarrow LL_{0(1)}$ ,  $LL_{-2(-1)} \rightarrow LL_{-1(2)}$  and  $LL_{-3(-2)} \rightarrow LL_{2(3)}$  in weakly n-doped graphene layers (Fig. 1c,d). On resonance with these transitions the induced transmission is enhanced. The strongest resonant enhancement (by factor of 2.5 relative to the signal at  $B = 0$ ) is observed for the energetically lowest transition (Fig. 1d). Note that owing to the vanishing density of states between LLs (for example, for  $1 \text{ T} < B < 3 \text{ T}$ ) the pump-probe signal is expected to vanish in this region. The observed non-zero signals in the experiment most likely stem from intraband LL transitions in the highly doped graphene layers close to the interface with the SiC substrate. In cw magneto-spectroscopy experiments, broad absorption features from doped layers have already been observed<sup>33,34</sup> supporting this interpretation.

For magnetic fields below 3 T the relaxation dynamics is characterized by a single exponential decay with a time constant of about 20 ps (Fig. 1b,e). For higher magnetic fields an additional fast decay component is observed. At  $B = 4.2$  T the  $LL_{-1(0)} \rightarrow LL_{0(1)}$  transition is resonantly excited. Here, we observe a fast initial decay of  $\tau = (3 \pm 1)$  ps—that is, the initial dynamics is almost one order of magnitude faster than the slow component. This very fast decay of the pump–probe signal is surprising, as the LL spacing does not match the energy of optical phonons and, thus, the carrier–phonon scattering is expected to be strongly quenched<sup>35,36</sup>.

To shed light on the nature of the observed fast population change responsible for the acceleration of the carrier dynamics, we employ circularly polarized radiation ( $\sigma^+$  and  $\sigma^-$ -radiation). We record DTS successively for all four combinations of pumping and probing with  $\sigma^+$  and  $\sigma^-$ -radiation (see Fig. 2a). According to the optical selection rules,  $\sigma^+$ -radiation pumps the  $LL_{-1} \rightarrow LL_0$  transition and  $\sigma^-$ -radiation the  $LL_0 \rightarrow LL_1$  transition<sup>37</sup> (see Fig. 2b). It is instructive to visualize the expected DTS sign in the absence of scattering for intrinsic graphene—that is, for initial occupations  $\rho_0 = 0.5$ ,  $\rho_{-1} = 1$  and  $\rho_1 = 0$ . This system is fully symmetric with respect to electrons and holes and, consequently, with respect to excitation by  $\sigma^+$  and  $\sigma^-$ -radiation. In this case, assuming that the dynamics is determined only by Pauli blocking, one expects positive DTS (increased transmission) for pumping and probing with the same polarization state and negative pump–probe signals (increased absorption) for pumping and probing with the opposite polarization state (see Fig. 2b). The signals within one pair of similar and opposite polarization feature similar amplitudes. For doped graphene the electron–hole symmetry is broken; hence, the absolute values of the induced transmission differ for the four different polarization combinations. Nevertheless, this does not change the expected DTS sign discussed above. Furthermore, energy relaxation via phonons and defect-mediated phonon scattering have no influence, as these processes relax the carrier distribution back into the equilibrium state.

The experiments show the following behaviour: the DTS for pumping with  $\sigma^-$ -radiation (Fig. 2c,e) exhibits a fast initial decay, of the order of the pulse duration, and a slower relaxation component. The sign of the DTS is in accord with the expectation considering the pump scheme depicted in Fig. 2b. In particular, negative DTS is observed for pumping with  $\sigma^-$ -radiation and probing with  $\sigma^+$ -radiation (Fig. 2e). For pumping with  $\sigma^+$ -radiation and probing with  $\sigma^-$ -radiation (Fig. 2g), however, an unexpected positive signal is observed, indicating that a strong redistribution of carriers must take place, beyond the effect induced by the photon field. A possible explanation is efficient Auger scattering, which can lead to a fast redistribution of carriers, giving rise to a different sign of the DTS. One can distinguish two counteracting Auger scattering processes, inducing  $LL_0 \rightarrow LL_{-1}$ ,  $LL_0 \rightarrow LL_1$  and  $LL_{-1} \rightarrow LL_0$ ,  $LL_1 \rightarrow LL_0$  transitions, respectively, as indicated in the sketches to the left of the panels containing the experimental data (Fig. 2c, e,g,i). Generally, they are referred to as Auger recombination and impact ionization, respectively. In graphene, the terminology is not straightforward, as  $LL_0$  is shared by the valence and the conduction bands. Therefore, in the following, we will refer to  $LL_0 \rightarrow LL_{-1}$  and  $LL_0 \rightarrow LL_1$  ( $LL_{-1} \rightarrow LL_0$  and  $LL_1 \rightarrow LL_0$ ) as outward (inward) Auger scattering with respect to the zeroth LL. Finally, the DTS for pumping with  $\sigma^+$ -radiation and probing with  $\sigma^+$ -radiation contains a negative tail after an initially positive peak (see Fig. 2i). Such a behaviour cannot be understood by just considering optical pumping and energy relaxation—again suggesting a crucial contribution from Auger scattering.

To obtain a thorough understanding of the underlying elementary scattering processes we performed microscopic calculations. Next, the foundation of the model is described, then we compare experimental and calculated DTS results and, finally,

we discuss the microscopic mechanism behind the experimentally observed and theoretically confirmed unexpected DTS behaviour. Our model is based on the density matrix formalism<sup>38,39</sup>. Similar to previous modelling in the absence of a magnetic field<sup>18,40</sup>, we derive a set of equations describing time-resolved microscopic polarizations  $p_{mn'}(t)$  and population probabilities  $\rho_n(t)$

$$\dot{\rho}_n(t) = \pm 2 \sum_{n'} \text{Re}[\Omega_{mn'}(t)p_{mn'}(t)] + S_n^{\text{in}}(t)[1 - \rho_n(t)] - S_n^{\text{out}}(t)\rho_n(t)$$

$$\dot{p}_{mn'}(t) = i\Delta\omega_{mn'}p_{mn'}(t) + \Omega_{mn'}(t)[\rho_n(t) - \rho_{n'}(t)] - \frac{\Gamma(t)}{\hbar}p_{mn'}(t)$$

Here  $\Omega_{mn'}(t)$  denotes the Rabi frequency,  $\Delta\omega_{mn'}$  the LL transition frequency,  $S_n^{\text{in/out}}(t)$  the time-dependent in- and out-scattering rates and  $\Gamma(t)$  the many-particle and disorder-induced dephasing of the microscopic polarization. The magnetic field was introduced into the Dirac equation via the Peierls substitution<sup>37</sup>. The equations include the optical excitation as well as Coulomb- and phonon-induced many-particle scattering processes. The strength of the carrier–light interaction is given by the optical matrix element and depends on the excitation field, both being incorporated into the Rabi frequency. The time- and LL-dependent in- and out-scattering rates  $S_n^{\text{in/out}}(t) = S_n^{\text{in/out}}|_{\text{Coulomb}}(t) + S_n^{\text{in/out}}|_{\text{phonon}}(t)$  describe energy-conserving many-particle Coulomb processes and inelastic scattering with phonons. The efficiency of the former is determined by the Coulomb matrix elements that are obtained using tight-binding wavefunctions. The microscopic treatment of the Coulomb interaction is crucial for understanding the experimentally observed fast carrier dynamics. In contrast, the carrier–phonon scattering is negligibly small at the beginning, owing to the mismatch of the optical phonon energy and the investigated inter-LL transitions. Scattering with acoustic phonons assisted by impurities is expected to contribute to the experimentally observed slower component in the differential transmission spectra (for details of modelling refer to Methods). The modelling was performed for low n-type graphene with a carrier concentration of  $6 \times 10^{10} \text{ cm}^{-2}$ , which corresponds a filling of  $LL_0$  of 64% at 4.2 T. (At  $B = 0$  this would correspond to a Fermi energy of 28 meV, see also Methods for details of sample doping.) First, we optically generate a non-equilibrium distribution by applying a circularly polarized pulse with a width of 2.7 ps, a pump fluence of  $0.1 \mu\text{J cm}^{-2}$  and an excitation energy of 75 meV, corresponding to the experimental realization. Then, we investigate the temporal evolution of the microscopic polarization  $p_{mn'}$  and the carrier occupations  $\rho_n(t)$  in the involved LLs. We focus on the carrier dynamics within the energetically lowest LLs.

The calculated differential transmission reproduces well all qualitative features of the measured DTS (see Fig. 2d,f,h,j). For pumping with  $\sigma^+$ -radiation, the theoretical curves show the same surprising result as observed in the experiment, namely the unexpected positive signal for probing with  $\sigma^-$ -radiation and the initially positive and subsequently negative signal for probing with  $\sigma^+$ -radiation (Fig. 2h,j). We note that by artificially weakening the electron–electron coupling the expected negative DTS is obtained for pumping and probing with opposite polarization (see Supplementary Methods), confirming that Auger processes are indeed the reason for the surprising positive DTS observed in the experiment, as further discussed below. Note that for pumping with  $\sigma^-$ -radiation, the signals are in accord with the expectations considering the optical selection rules; however, when probing with  $\sigma^+$ -radiation a plateau after the initial peak is observed in the DTS (Fig. 2f). This is an indication that also in this configuration the underlying dynamics is more complex than a simple relaxation to the equilibrium. The processes leading to the plateau are further discussed in the Supplementary Methods.

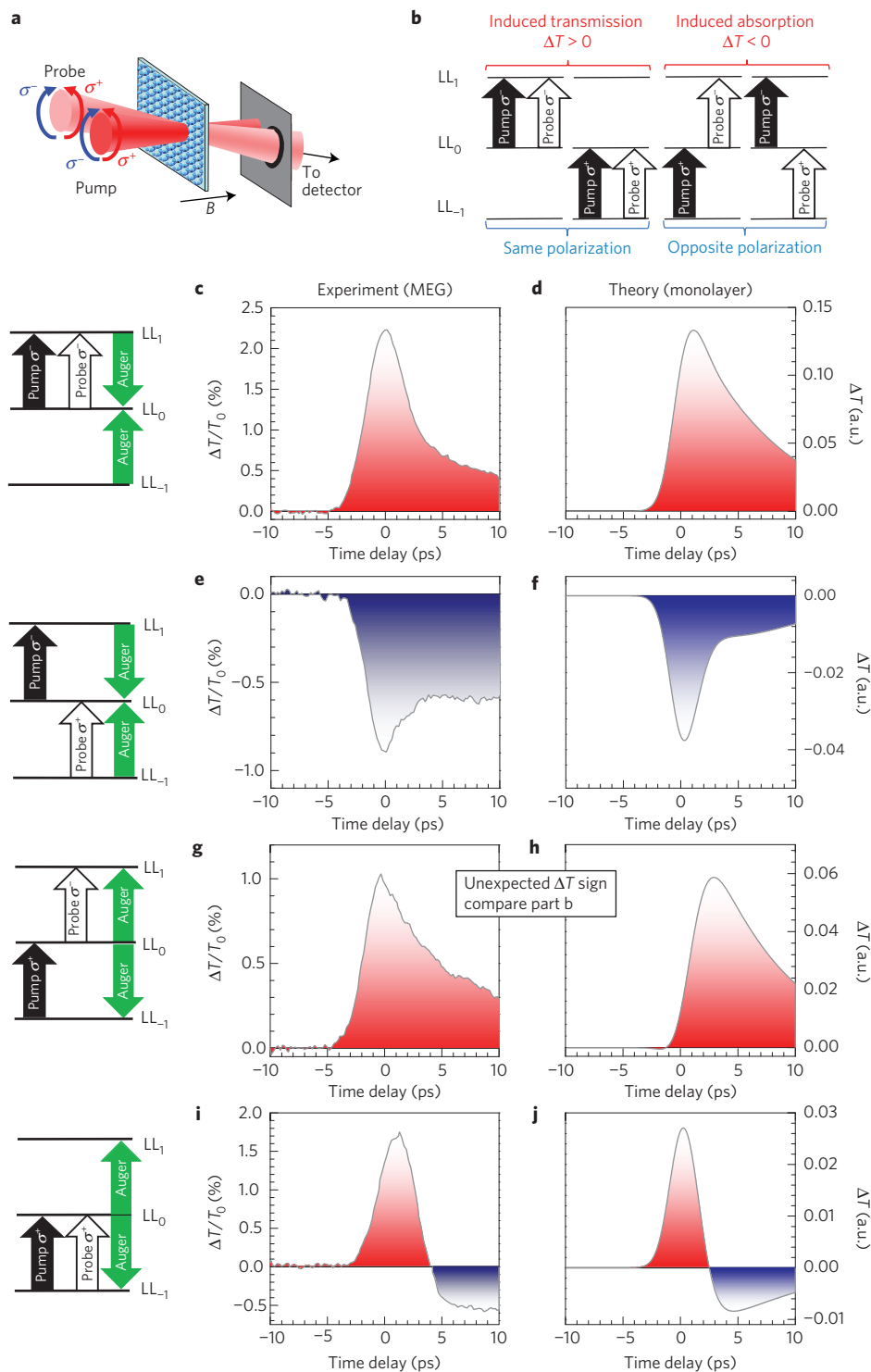


**Figure 2 | Pump-probe spectroscopy on graphene with circularly polarized radiation.** **a**, Configuration of the experiments for pumping and probing with  $\sigma^-$  and  $\sigma^+$ -radiation. **b**, In the absence of strong Auger scattering, pumping and probing with the same polarization results in induced transmission, whereas applying opposite polarization results in induced absorption. **c,e,g,i**, Experimental pump-probe signals for all four combinations of pumping and probing with  $\sigma^-$  and  $\sigma^+$ -radiation. Blue and red shaded regions highlight positive and negative DTS, respectively. **d,f,h,j**, Differential transmission calculated by microscopic theory for all four combinations of pumping and probing with  $\sigma^-$  and  $\sigma^+$ -radiation. The diagrams left of panels **c-j** indicate the corresponding polarization of pump and probe beam as well as the dominating Auger scattering process—that is, either inward or outward Auger scattering. The photon energy is 75 meV and  $B=4.2$  T for all panels. a.u., arbitrary units.

As our calculations give microscopic access to the time-resolved populations of the LLs, we can reveal the underlying elementary scattering processes responsible for the observed and theoretically predicted surprising features in the differential transmission

spectra. Our calculations clearly reveal that Auger processes play the crucial role. They give rise to an efficient redistribution of carriers in the energetically equidistant levels LL<sub>0</sub>, LL<sub>1</sub> and LL<sub>-1</sub>. The time-resolved occupations of the energetically lowest LLs are

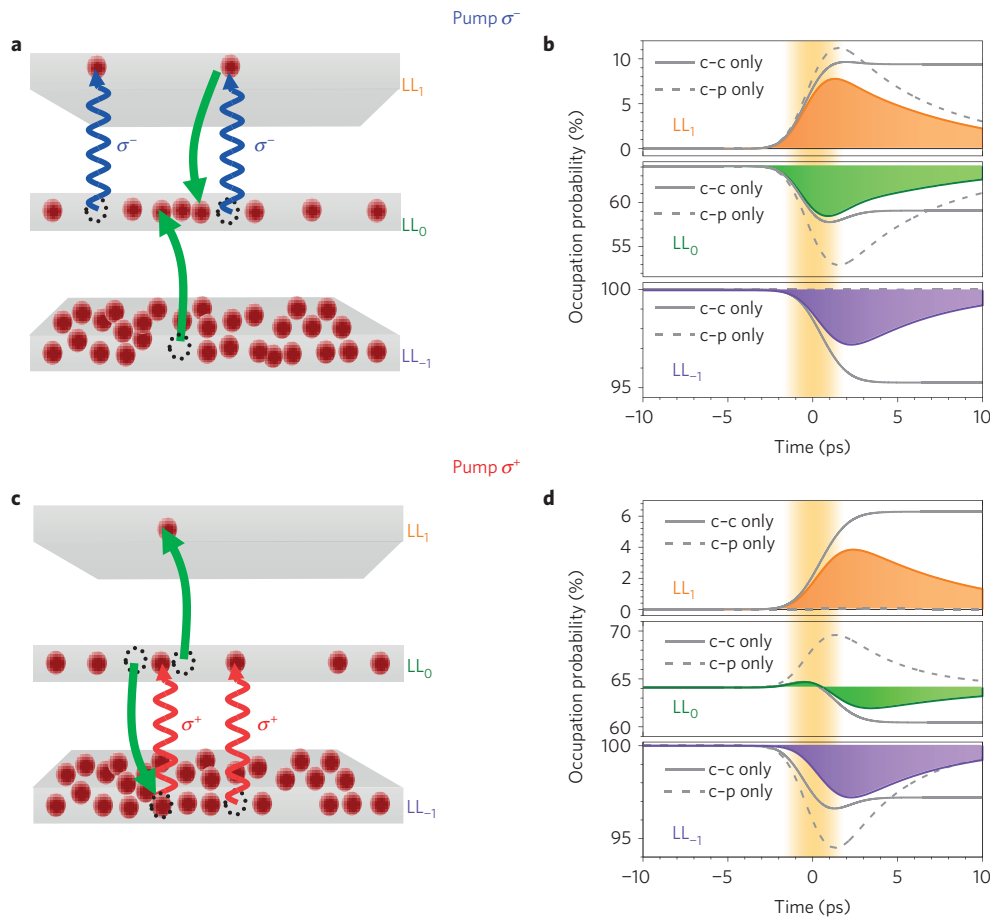


**Figure 3 | Level occupation for pumping with circularly polarized radiation.** **a,c**, Illustration of the transitions between  $LL_{-1}$ ,  $LL_0$  and  $LL_1$  induced by optical pumping and the net Auger scattering. The green arrows symbolize the predominant contribution of inward (**a**) or outward (**c**) Auger scattering. **b,d**, Occupations of the LLs corresponding to **a** and **c**, respectively, calculated by microscopic modelling, taking into account the optical excitation, carrier-carrier and carrier-phonon scattering (coloured curves). The solid (dashed) grey line corresponds to the dynamics considering optical excitation and carrier-carrier (carrier-phonon) scattering only. The vertical orange shaded area indicates the duration of the pump pulse.

shown in Fig. 3: for pumping with  $\sigma^-$ -radiation, optical excitation depopulates  $LL_0$ , leading to a decrease of  $\rho_0(t)$  (Fig. 3b). At the same time,  $LL_1$  becomes populated, resulting in an increase of  $\rho_1(t)$ . In the case of pumping with  $\sigma^-$ -radiation, inward Auger scattering dominates, because it counteracts the optical pumping (Fig. 3a). This effect causes the decreased occupation of  $LL_{-1}$ , which is not affected by the optical pumping (Fig. 3b). In contrast, for pumping with  $\sigma^+$ -radiation, outward Auger scattering dominates over inward processes (Fig. 3c). In n-type graphene, the Auger scattering is so efficient that, after an initial increase of  $\rho_0(t)$  due to the optical pumping, an Auger-induced decrease is found (Fig. 3d). As a result, we do not observe enhanced absorption and negative DTS as expected for pumping with  $\sigma^+$  and probing with  $\sigma^-$ -radiation (Fig. 2b), but rather a positive pump-probe signal (see Fig. 2g,h). The Auger scattering efficiently populates  $LL_1$ , giving rise to absorption bleaching of the  $\sigma^-$ -probe pulse and resulting in positive differential transmission. The initial increase and subsequent decrease of the occupation of  $LL_0$  is responsible for the sign reversal of the DTS for pumping and probing with  $\sigma^+$ -radiation (see Fig. 2i,j; for a detailed explanation see Supplementary Methods).

It is instructive to separately consider the effects of carrier-carrier and carrier-phonon scattering on the level occupation (see grey lines in Fig. 3b,d). Pure carrier-phonon scattering leads to population changes only in the LLs that are directly affected by the optical pumping. Consequently, in this case the population of  $LL_0$  is

increased by  $\sigma^+$  pumping (Fig. 3d). In contrast, pure carrier-carrier scattering results in a dynamics that is qualitatively very similar to the full dynamics. The only difference is that without phonon scattering the level occupation does not relax back to the initial equilibrium state, because the energy added by the pump pulse cannot be removed from the electronic system. This leads to a new hot-carrier equilibrium state that is characterized by a decreased population of both  $LL_{-1}$  and  $LL_0$  as well as an increased population in  $LL_1$  for pumping with both  $\sigma^-$  and  $\sigma^+$  radiation (Fig. 3b,d).

Note that for intrinsic graphene the effect of the Auger processes on the carrier distribution is not strong enough to change the sign of the DTS. Even small doping breaks the electron-hole symmetry and, consequently, the balance between outward and inward Auger scattering. This results in the surprising effects observed. The same effects observed for n-doped graphene under pumping with  $\sigma^+$ -radiation occur for p-doped graphene under pumping with  $\sigma^-$ -radiation. Further reasoning behind the unexpected DTS sign in Fig. 2g can be given using simple thermodynamic arguments. The observed Auger scattering represents a very efficient (elastic) relaxation process that drives the system perturbed by the pump pulse towards the new equilibrium at higher electron temperature. This redistribution is visible, in particular, in the occupation of  $LL_0$ , which increases with increasing electron temperature for p-doped graphene, but always decreases in the n-doped system. Counter-intuitively, the latter happens even when  $LL_0$  is directly pumped. The positive DTS sign for a  $\sigma^-$ -polarized probe pulse in Fig. 2g

thus directly reflects the pump-induced depopulation of  $LL_0$ . More detailed considerations described in the Supplementary Methods reveal that positive DTS signals for  $\sigma^-$ -polarized probe pulses are expected when the initial occupation of  $LL_0$  exceeds a threshold value of  $2 - \sqrt{2} \approx 0.59$ .

Our study conclusively shows that carrier–carrier scattering is the predominant mechanism for carrier redistribution in Landau-quantized graphene. Scattering with optical phonons, on the other hand, is expected to be strongly suppressed unless the LLs are resonant with the optical phonon energy<sup>35,36</sup>. In the experiments performed, we find only a moderate increase of the decay time with increasing magnetic field, from  $18 \pm 3$  ps at 0 T to  $22 \pm 3$  ps at 3 T (Fig. 1b,e). A possible explanation for this decay component could be defect-assisted scattering with acoustic phonons, which has been identified as an important scattering mechanism in the absence of magnetic fields<sup>41,42</sup>. The role of these phonon-related relaxation channels for Landau-quantized graphene still needs to be thoroughly investigated in future studies.

In conclusion, our results show that Landau-quantized graphene is ideal for the investigation of strong carrier–carrier scattering processes. The levels  $LL_{-1}$ ,  $LL_0$  and  $LL_1$  are decoupled from the remaining spectrum both with respect to optical excitation and scattering. The three equidistant but optically selectively addressable levels are an ideal system to study energy-conserving carrier–carrier scattering processes. The possibility of polarization-sensitive induced absorption and induced transmission can be applied for concepts of optical switching with high functionality. In quantum information processing, circularly polarized radiation is often used to address quantum bits. The switching in Landau-quantized graphene can be controlled all-optically by the polarization state of the radiation. Electric gating allowing one to switch from n-type to p-type graphene would add even more functionality. Furthermore, the non-equidistant Landau spectrum of graphene offers the possibility of developing a tunable laser. For example, pumping the  $LL_{-3} \rightarrow LL_2$  transition should result in population inversion between  $LL_2$  and  $LL_1$ . On the other hand, Auger scattering may be directly exploited to realize carrier multiplication in Landau-quantized graphene. To this end, pumping the  $LL_{-3} \rightarrow LL_4$  transition Auger scattering between the equidistant levels  $LL_4$ ,  $LL_1$  and  $LL_0$  can facilitate carrier multiplication.

## Methods

**Pump–probe spectroscopy.** The free-electron laser FELBE provided frequency-tunable Fourier-limited radiation pulses. In the experiments described in the paper a photon energy of 75 meV was chosen. The pulse duration of the 75-meV pulses was 2.7 ps (repetition rate 13 MHz). The pulses were split into pump and probe pulses by a pellicle beam splitter. The polarizations of pump and probe beams were controlled independently. Frequency-tunable quarter-wave plates (from Alphalas GmbH) were used for the generation of circularly polarized radiation. Both the pump and probe beam were focused on the sample in the magnet cryostat by an off-axis parabolic mirror (effective focal length: 178 mm). The spot size on the sample was  $\sim 0.5$  mm (FWHM). The pump fluence was  $\sim 0.1 \mu\text{J cm}^{-2}$ —in this range the DTS increased linearly with pump fluence. The fluence of the probe beam was about 10% of the pump fluence. The time delay between pump and probe pulses was varied by a mechanical delay stage.

**Microscopic modelling.** In this study, we focus on the impact of Coulomb interactions and include carrier–phonon scattering on a phenomenological level. To this end, the full scattering rate  $S_n^{\text{in/out}}|_{\text{phonon}}$  including Pauli-blocking terms and phonon occupations is considered, while the corresponding electron–phonon matrix elements are adjusted to the experimentally observed decay. The phonons are assumed to be in equilibrium with a phonon bath and their occupations are described by the Bose–Einstein distribution. In contrast, the Coulomb interaction is entirely considered on a microscopic footing. We also take dynamical screening of the Coulomb potential into account by evaluating the dielectric function  $\varepsilon(q, \omega)$  in the random phase approximation, following the approach of refs 37,43. The LL broadening is calculated self-consistently, taking into account scattering of electrons on an impurity potential with a Gaussian white noise distribution<sup>44</sup>. This electron-impurity scattering yields the dominant contribution to the

dephasing  $\Gamma(t)$  of the microscopic polarization, which also comprises contributions of Coulomb- and phonon-induced many-particle scattering.

**Sample doping.** MEG samples grown on the C-terminated face of SiC consist of a number of layers that are rotated against each other. Charge transfer from the SiC substrate results in high doping of the first layer at the interface, with an electron concentration of  $10^{13} \text{ cm}^{-2}$ . Successive layers exhibit a doping of  $\sim 30\%$  of the previous layer; hence, after five layers, low carrier concentrations in the range  $10^{10} \text{ cm}^{-2}$ – $10^{11} \text{ cm}^{-2}$  are reached<sup>16,31</sup>. Pump–probe experiments, cw magneto-spectroscopy and angle-resolved photoemission spectroscopy indicate that a substantial number of layers exhibit doping in the region of  $10^{10} \text{ cm}^{-2}$  (refs 9,18,45). For the sample used in our experiment, layers with carrier concentrations of  $\sim 10^{10} \text{ cm}^{-2}$  were evidenced by magneto-spectroscopy and pump–probe experiments. The experiments in all four combinations of pumping and probing with  $\sigma^+$ - and  $\sigma^-$ -radiation in magnetic fields directly indicate that  $LL_0$  can be neither completely filled nor completely empty. The completely filled zeroth LL would give  $4.1 \times 10^{11} \text{ cm}^{-2}$  electrons for  $B=4.2$  T. For  $B=0$  this corresponds to a Fermi energy of 53 meV. Note that intrinsic graphene is characterized by  $\rho_0=0.5$ , corresponding to  $2.0 \times 10^{11} \text{ cm}^{-2}$  electrons at  $B=4.2$  T. For the microscopic modelling a concentration of excess electrons of  $6 \times 10^{10} \text{ cm}^{-2}$  was used. This value corresponds to a total of  $2.6 \times 10^{11} \text{ cm}^{-2}$  electrons in  $LL_0$ ,  $\rho_0 = (2.6 \times 10^{11}) / (4.1 \times 10^{11}) = 0.64$  and a Fermi energy (at  $B=0$ ) of 28 meV. This doping value, being in between the experimentally determined borders, provides an overall good agreement between experimental and calculated DTS. By varying the carrier concentration in the calculation, individual features of the DTS change slightly; however, the surprising DTS sign change remains. The experimental signals contain contributions from graphene of different doping due to the gradient in doping towards the substrate. Furthermore, there are slight lateral inhomogeneities, which are averaged owing to the applied infrared beams having a diameter of  $\sim 0.5$  mm.

Received 20 March 2014; accepted 20 October 2014;  
published online 24 November 2014

## References

- Drexler, C. *et al.* Magnetic quantum ratchet effect in graphene. *Nature Nanotech.* **8**, 104–107 (2013).
- Ponomarenko, L. A. *et al.* Cloning of Dirac fermions in graphene superlattices. *Nature* **497**, 594–597 (2013).
- Dean, C. R. *et al.* Hofstadter's butterfly and the fractal quantum Hall effect in moire superlattices. *Nature* **497**, 598–602 (2013).
- Hunt, B. *et al.* Massive Dirac fermions and Hofstadter butterfly in a van der Waals heterostructure. *Science* **340**, 1427–1430 (2013).
- Bolotin, K. I., Ghahari, F., Shulman, M. D., Stormer, H. L. & Kim, P. Observation of the fractional quantum Hall effect in graphene. *Nature* **462**, 196–199 (2009).
- Du, X., Skachko, I., Duerr, F., Luican, A. & Andrei, E. Y. Fractional quantum Hall effect and insulating phase of Dirac electrons in graphene. *Nature* **462**, 192–195 (2009).
- Novoselov, K. S. *et al.* Two-dimensional gas of massless Dirac fermions in graphene. *Nature* **438**, 197–200 (2005).
- Zhang, Y., Tan, J. W., Stormer, H. L. & Kim, P. Experimental observation of the quantum Hall effect and Berry's phase in graphene. *Nature* **438**, 201–204 (2005).
- Sadowski, M. L., Martinez, G., Potemski, M., Berger, C. & deHeer, W. A. Landau level spectroscopy of ultrathin graphene layers. *Phys. Rev. Lett.* **97**, 266405 (2006).
- Plochocka, P. *et al.* High energy limit of massless Dirac fermions in multilayer graphene using magneto-optical transmission spectroscopy. *Phys. Rev. Lett.* **100**, 087401 (2008).
- Orlita, M. *et al.* Approaching the Dirac point in high-mobility multilayer epitaxial graphene. *Phys. Rev. Lett.* **101**, 267601 (2008).
- Neugebauer, P., Orlita, M., Faugeras, C., Barra, A.-L. & Potemski, M. How perfect can graphene be? *Phys. Rev. Lett.* **103**, 136403 (2009).
- Crassee, I. *et al.* Giant Faraday rotation in single- and multilayer graphene. *Nature Phys.* **7**, 48–51 (2011).
- Kawano, Y. Wide-band frequency tunable terahertz and infrared detection with graphene. *Nanotechnology* **24**, 21404 (2013).
- Dawlaty, J. M., Shivaraman, S., Chandrashekar, M., Rana, F. & Spencer, M. G. Measurement of ultrafast carrier dynamics in epitaxial graphene. *Appl. Phys. Lett.* **92**, 042116 (2008).
- Sun, D. *et al.* Ultrafast relaxation of excited Dirac fermions in epitaxial graphene using optical differential transmission spectroscopy. *Phys. Rev. Lett.* **101**, 157402 (2008).
- Breusing, M. *et al.* Ultrafast nonequilibrium carrier dynamics in a single graphene layer. *Phys. Rev. B* **83**, 153410 (2011).

18. Winnerl, S. *et al.* Carrier relaxation in epitaxial graphene photoexcited near the Dirac point. *Phys. Rev. Lett.* **107**, 237401 (2011).
19. Brida, D. *et al.* Ultrafast collinear scattering and carrier multiplication in graphene. *Nature Commun.* **4**, 1987 (2013).
20. Tielrooij, K. J. *et al.* Photoexcitation cascade and multiple hot-carrier generation in graphene. *Nature Phys.* **9**, 248–252 (2013).
21. Plochocka, P. *et al.* Slowing hot-carrier relaxation in graphene using a magnetic field. *Phys. Rev. B* **80**, 245415 (2009).
22. Foster, M. S. & Aleiner, I. L. Slow imbalance relaxation and thermoelectric transport in graphene. Quasiclassical cyclotron resonance of Dirac fermions in highly doped graphene. *Phys. Rev. B* **79**, 085415 (2010).
23. Otsuji, T. *et al.* Graphene-based devices in terahertz science and technology. *J. Phys. D* **45**, 303001 (2012).
24. Rana, F. Electron–hole generation and recombination rates for Coulomb scattering in graphene. *Phys. Rev. B* **76**, 155431 (2007).
25. Winzer, T., Knorr, A. & Malic, E. Carrier multiplication in graphene. *Nano Lett.* **10**, 4839–4843 (2010).
26. Winzer, T. & Malic, E. Impact of Auger processes on carrier dynamics in graphene. *Phys. Rev. B* **85**, 241404 (2012).
27. Gierz, I. *et al.* Snapshots of non-equilibrium Dirac carrier distributions in graphene. *Nature Mater.* **12**, 1119–1124 (2013).
28. Johannsen, J. C. *et al.* Direct view of hot carrier dynamics in graphene. *Phys. Rev. Lett.* **111**, 027403 (2013).
29. Berger, C. *et al.* Electronic confinement and coherence in patterned epitaxial graphene. *Science* **312**, 1191–1196 (2006).
30. Ferrari, A. C. *et al.* Raman spectrum of graphene and graphene layers. *Phys. Rev. Lett.* **97**, 187401 (2006).
31. Sun, D. *et al.* Spectroscopic measurement of interlayer screening in multilayer epitaxial graphene. *Phys. Rev. Lett.* **104**, 136802 (2010).
32. Winnerl, S. *et al.* Time-resolved spectroscopy on epitaxial graphene in the infrared spectral range: Relaxation dynamics and saturation behaviour. *J. Phys. Condens. Matter* **25**, 054202 (2013).
33. Witowski, A. M. *et al.* Quasiclassical cyclotron resonance of Dirac fermions in highly doped graphene. *Phys. Rev. B* **82**, 165305 (2010).
34. Orlita, M. *et al.* Classical to quantum crossover of the cyclotron resonance in graphene: A study of the strength of intraband absorption. *New J. Phys.* **14**, 095008 (2012).
35. Wang, Z.-W. *et al.* The temperature dependence of optical phonon scattering in graphene under strong magnetic field. *J. Phys. Soc. Jpn* **82**, 094606 (2013).
36. Wandler, E., Knorr, A. & Malic, E. Resonant carrier-phonon scattering in graphene under Landau quantization. *Appl. Phys. Lett.* **103**, 253117 (2013).
37. Goerbig, M. O. Electronic properties of graphene in a strong magnetic field. *Rev. Mod. Phys.* **83**, 1193–1243 (2011).
38. Haug, H. & Koch, S. W. *Quantum Theory of the Optical and Electronic Properties of Semiconductors* (World Scientific, 2009).
39. Malic, E. & Knorr, A. *Graphene and Carbon Nanotubes – Ultrafast Relaxation Dynamics and Optics* (Wiley-VCH, 2013).
40. Malic, E., Winzer, T., Bobkin, E. & Knorr, A. Microscopic theory of absorption and ultrafast many-particle kinetics in graphene. *Phys. Rev. B* **84**, 205406 (2011).
41. Graham, M. W., Shi, S. F., Ralph, D. C., Park, J. & McEuen, P. L. Photocurrent measurements of supercollision cooling in graphene. *Nature Phys.* **9**, 103–108 (2013).
42. Betz, A. C. *et al.* Supercollision cooling in undoped graphene. *Nature Phys.* **9**, 109–112 (2013).
43. Roldán, R., Goerbig, M. O. & Fuchs, J.-N. The magnetic field particle-hole excitation spectrum in doped graphene and in a standard two-dimensional electron gas. *Semicond. Sci. Technol.* **25**, 034005 (2010).
44. Ando, T. & Uemura, Y. Theory of quantum transport in a two-dimensional electron system under magnetic fields. I. Characteristics of level broadening and transport under strong fields. *J. Phys. Soc. Jpn* **36**, 959–967 (1974).
45. Sprinkle, M. *et al.* First direct observation of a nearly ideal graphene band structure. *Phys. Rev. Lett.* **103**, 226803 (2009).

### Acknowledgements

Support from the German Science Foundation DFG in the framework of the Priority Program 1459 Graphene is acknowledged. E.M. and F.W. are grateful to the Einstein Foundation Berlin. The research at the free-electron laser FELBE was supported by the European Community's Seventh Framework Programme (FP7/2007–2013) under Grant agreement No. 226716. Part of this work has been supported by the ERC-2012-AdG-320590 MOMB project as well as the EC Graphene Flagship. We are grateful to P. Michel and the FELBE team for their dedicated support. The Grenoble group acknowledges fruitful discussions with D. M. Basko.

### Author contributions

S.W., M.M., M.H., M.O. and M.P. conceived the experiments; M.M. performed the experiments, partly together with M.O. and S.W.; M.M., S.W., H.S. and M.H. analysed and interpreted the data; F.W., E.M. and A.K. developed the microscopic theoretical model. M.O. and M.P. originated the considerations for critical level occupation described in the Supplementary Methods. C.B. and W.A.d.H. prepared the samples; S.W. and E.M. wrote the paper with major input and edits from M.H. All authors discussed the results and commented on the manuscript.

### Additional information

Supplementary information is available in the [online version of the paper](#). Reprints and permissions information is available online at [www.nature.com/reprints](http://www.nature.com/reprints). Correspondence and requests for materials should be addressed to M.M. or S.W.

### Competing financial interests

The authors declare no competing financial interests.